AIAA SciTech Forum
6-10 January 2020, Orlando, FL
AIAA Scitech 2020 Forum

10.2514/6.2020-0803

Stepped Wings at Moderate Re with Implications on Multipoint Wing Design

Yohanna G. T. Hanna*
University of Southern California, Los Angeles, CA 90089, USA

Mark N. West†
Concepts-to-Systems, Inc., Danville, VA 24540, USA

Jayanth N. Kudva‡
NextGen Aeronautics, Inc., Torrance, CA 90275, USA

Geoffrey R. Spedding§
University of Southern California, Los Angeles, CA 90089, USA

For chord-Reynolds numbers $10^4 \leq \mathrm{Re} \leq 10^5$ typical of small UAVs, the aerodynamics of airfoils and finite wings yield nonlinearities in the lift curve and are sensitive to small perturbations in the flow and/or geometry. These sensitivities at once make measurement, prediction and control difficult and at the same time allow for new control strategies. The design space of small wings can readily expand to unusual geometries and mechanisms, and as advanced materials are developed, there is renewed interest in large- and small-amplitude shape changing properties. In a project designed to explore the effect of large wing surface area changes, a set of spring-mounted, telescoping wings was developed. Absent any special matching shield, the neighboring segments on such a wing then introduce stepwise discontinuities in thickness and chord. Here, direct force balance data and PIV flow measurements of continuous, 3 step, and 7 step wings were made at $\mathrm{Re} \approx 74,000$. The results showed no adverse effect of the stepped geometry. Since the boundary-layers were deliberately tripped, the findings may extend to much higher Re.

I. Nomenclature

$\mathcal{AR}$	=	aspect ratio
b	=	span [m]
c	=	chord [m]
$\overline{c}$	=	mean aerodynamic chord [m]
c_r	=	root chord [m]
c_t	=	tip chord [m]
C_D	=	drag coefficient
C_L	=	lift coefficient
D	=	drag force [N]
L	=	lift force [N]
ℓ	=	local lift per unit span [N/m]
L/D	=	lift to drag ratio
q	=	dynamic pressure [N/m^2]
Re	=	Reynolds number
Re_x	=	Reynolds number as a function of x
S	=	planform area [m^2]
t	=	airfoil thickness [m]
U	=	freestream velocity [m/s]
$\overline{u}$	=	time-averaged velocity in x [m/s]
$\overline{v}$	=	time-averaged velocity in y [m/s]
$\overline{w}$	=	time-averaged velocity in z [m/s]
x	=	streamwise direction [m]
y	=	spanwise direction [m]
z	=	cross-stream direction [m]
α	=	angle of attack [°]
Γ	=	circulation [m^2/s]
δ	=	boundary layer thickness [m]
ν	=	kinematic viscosity [m^2/s]
ρ	=	density [kg/m^3]
ω_x	=	streamwise vorticity [1/s]

*Graduate Student, Department of Aerospace and Mechanical Engineering, AIAA Student Member
†Senior Engineer, AIAA Member
‡Principal Engineer, AIAA Fellow
§Professor, Department of Aerospace and Mechanical Engineering, AIAA Member

II. Introduction

As small unmanned aerial vehicles (UAV), high altitude aircraft, and wind turbines become more prevalent, the interest in wings occupying a Re regime between 10^4 and 10^5 has grown[1–3]. Part of the difficulty of studying airfoils in this moderate Re regime is the large disagreement in experimental data between facilities[4]. These discrepancies arise from sensitivities to wind tunnel turbulence levels, model contour accuracy, and model surface roughness[5]. Additionally, a large fraction of airfoils in literature exhibit multi-valued, non-monotonic $C_{\mathrm{L}}(\alpha)$ and $C_{\mathrm{D}}(\alpha)$ curves[4, 6–8].

In contrast to engineered flying devices, natural fliers are characterized by flexible, shape changing wings. Wind tunnel experiments of living and deceased birds as well as free flight observations have shown that birds continuously adjust their planform for varying flight conditions[9–11]. Similar shape changes may be advantageous to modern aircraft. Though research aircraft have implemented bio-inspired shape changes using feather like structures[12], distinctly non-biomimetic, telescoping wings may represent a mechanically-feasible solution to the numerous possible mechanisms for flight envelope extension[13, 14].

A typical telescoping wing design leads to stepwise discontinuities in the planform. Initial experiments suggest that the aerodynamic effects may be small[15, 16] while maintaining controllability[17, 18]. These results seem to have empirical support in observations on the lifting and/or propulsive wings/fins of certain birds and marine life. Humpback whales (*Megaptera novaengliae*), for example, have regular scallops on their flipper leading edge. It is hypothesized that these structures not only do no harm, but also induce streamwise vorticity which re-energizes the boundary layer, thus delaying separation[19].

This paper will present the results of an experimental study on stepped wing geometries at moderate Re in a low-turbulence wind tunnel. The force balance and PIV measurement sensitivities are sufficient to measure small (or large) differences in integrated forces, or local flow fields that may occur.

III. Materials and Methods

A. Wind Tunnel Testing

All experiments were conducted in the low-speed Dryden Wind Tunnel at USC. The low turbulence level of < 0.035% for frequencies between 10 and 1000 Hz for mean speeds between 4 and 20 m/s are due to the long, gradual 8:1 ratio converging section downstream of 11 anti-turbulence screens. The test section, as seen in Fig. 1, is octagonal with a width of 1.37 m. Flow speed was set to 12.7 m/s, yielding a chord-based Reynolds number of $\mathrm{Re} = U\bar{c}/\nu = 73,700 \approx 74,000$. From projected areas the blockage in the test section was estimated to be 2.5% so the comparative data were not corrected.

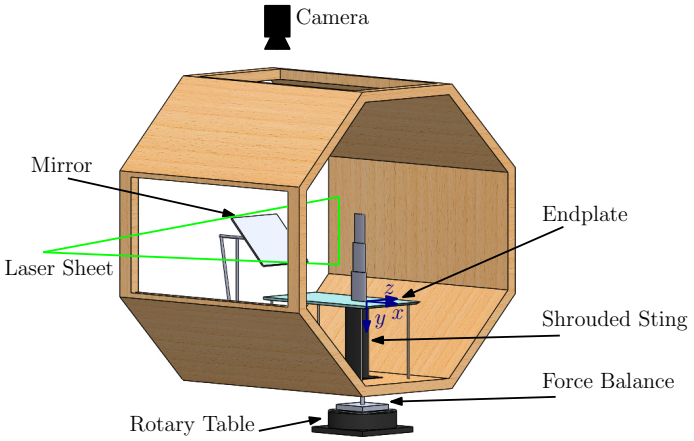

Fig. 1 Wind tunnel test section with force balance and PIV experimental setup. The mirror was not present during force balance experiments, and the balance was removed for PIV.

Three half-span wings were 3D printed using PLA filament on a Raise3D Pro2 Plus, which has a 12.5 µm x/y resolution and 10 µm layer thickness. All wings had a NACA 0012 profile with $c_r = 10$ cm and $c_t = 7$ cm, root and tip

chords respectively, and $b = 42$ cm, span. The configurations considered were 3 steps, 7 steps, and continuous, as shown in Fig. 2a. Wing sections were arranged such that the thickest portion of the wing, or $0.3c$, was at a constant x location along y. For stepped wings, the wing was sectioned into rectangular segments of equal span, while the continuous wing had a trapezoidal planform. Such geometric constraints meant that all wings had the same planform area, S, of 357.0 cm^2 and aspect ratio, AR. From

$$\mathit{AR} = \frac{b^2}{S} , \tag{1}$$

the semispan $\mathit{AR} = 2.5$ for all models. The mean aerodynamic chord, $\overline{c}$, is

$$\overline{c} = \frac{2}{S}\int_0^{b/2} c^2(y)\mathrm{d}y , \tag{2}$$

and was evaluated to 8.7 ± 0.1 cm for all models. An 8 mm steel rod was epoxied into each wing at $\overline{c}/4$, which also corresponded with $c_r/4$, to mount the models within the tunnel.

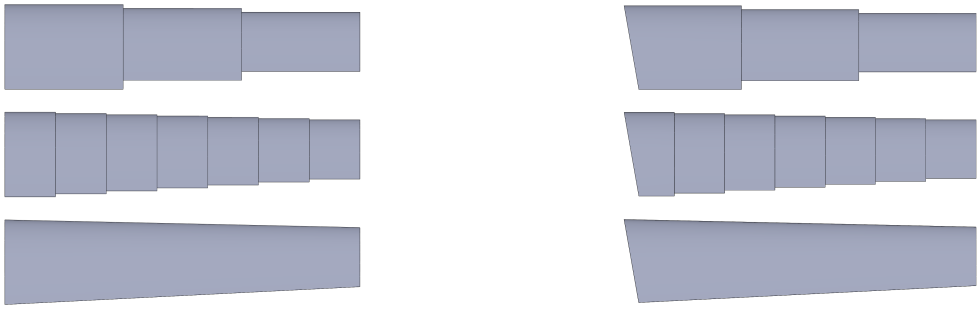

a) b)

Fig. 2 3D printed wings a) without and b) with sweep. Note that mounting rods are not shown.

To replicate a sideslip angle, three additional models were printed on the same 3D printer. Pictured in Fig. 2b, the geometry from the first set of experiments was swept by 10° from the leading edge and the corresponding area removed from the wing. The new area was approximately $S = 348.3$ cm^2. Swept models were arranged on the print bed so that layers were deposited in the same orientation as the unswept models so as to keep the direction of surface roughness similar.To ensure forces were applied at a similar location with respect to the force balance, the 8 mm steel mounting rod was placed at $\overline{c}/4$, which was further aft than $c_r/4$.

Because experiments were conducted at a moderate Re, the top surface of all six wings were tripped at $0.1c$. Based on flat plate estimates, the laminar boundary layer $\delta = 4.91x/\mathrm{Re}_x{}^{1/2} = 0.53$ mm at the root chord trip location. Boundary layer trips were created by layering 8 strips of 0.07 mm thick tape so the trip height was 0.56 mm or 1.05δ at the wing root. The tape had a width of 6.30 mm, or $0.60t$, where t is the maximum chord thickness at $\overline{c}$.

To create a quasi-full-span flow, an endplate was mounted at the root of the wing, as seen in Fig.1. The endplate had dimensions of $8.18\overline{c}$ in x by $4.09\overline{c}$ in z and a thickness of $0.15\overline{c}$. To allow for the mounting rod, a slot in the plate was placed at $2.48\overline{c}$ in x and at the center in z. Based on the longest distance from the leading edge of the end plate to the leading edge of the model, δ was estimated to be 2.3 mm. The gap between the model and the endplate was less than 1 mm, or 0.43δ.

B. Force Balance Calibration and Measurements

A custom cruciform force balance, described in Ref. [20], was mounted on top of a rotary table, which would set angle of attack, α. This assembly was placed underneath the tunnel, with a sting running from the top of the balance through the floor of the tunnel. The portion of the sting within the tunnel was shrouded from flow, as shown in Fig. 1. At the beginning of each testing day, at least one calibration was completed generating a 3-by-4 calibration matrix. To reduce random error from the calibration procedure, the 3 most recent calibration matrices were averaged together, and the averaged matrix was used for all measurements. The balance uncertainty in the axial and normal directions were less than 5 mN and 15 mN, respectively.

Zeroing forces corresponding to the weight of the model were taken before each experiment. Each experiment consisted of 5 forward and backward α sweeps from $\alpha = -3°$ to 15° in 1° increments. To allow for transients to settle, measurements were taken 10 s after α was changed. The sampling rate was 1 kHz and data were taken for 10 s and averaged to produce a single measurement. The average of 10 such measurements produced a single data point for a given α. The maximum of the measurement standard deviation, precision, and device uncertainty was considered the uncertainty of the data point. Lift, L, and drag, D, forces were nondimensionalized by S and the dynamic pressure, q

$$q = \frac{1}{2}\rho U^2 \,, \tag{3}$$

yielding

$$C_\mathrm{L} = \frac{L}{qS} \tag{4}$$

and

$$C_\mathrm{D} = \frac{D}{qS} \,. \tag{5}$$

C. Particle Image Velocimetry Measurements

To conduct PIV measurements, the tunnel was filled with a glycerin-based smoke with particle diameters typically 0.2-0.3 µm. Images were acquired with a LaVision Imager sCMOS camera, which has 2560×2160 16-bit pixels, mounted with a Nikon 50 mm NIKKOR lens. As shown in Fig. 1, a laser sheet was generated by a Quantel EverGreen double-pulsed Nd:YAG laser and the image was reflected into the camera by a 30 cm by 30 cm mirror mounted 66 cm, $7.6\overline{c}$, downstream of the model trailing edge. Total blockage is estimated to be 7.3% of total test section area. The laser sheet was position 6.5 cm downstream of the model, or $0.75\overline{c}$. The camera field of view in relation to the wing is shown in Fig. 3.

200 image pairs were captured for $\alpha = 5°$ and 9° and each wing configuration at a sample rate of 9.6 Hz and time delay of 250 µs. To obtain velocity field estimates, images were processed in LaVision's DaVis software. A multi-pass algorithm with two initial passes of 48×48 pixel interrogation windows and three passes with window size of 32×32 pixels. 50% window overlap gave a spatial resolution of 16 pixels, which is 1.88 mm or $0.022\overline{c}$. The 200 instantaneous vector fields were averaged to create a time-averaged velocity field. The uniform background flow was subtracted leaving just the time-averaged perturbation velocities, $\overline{v}$ and $\overline{w}$. Streamwise vorticity, $\omega_x = \frac{\partial \overline{w}}{\partial y} - \frac{\partial \overline{v}}{\partial z}$, was calculated in MATLAB using the built-in function curl. To reduce low level noise, vorticity fields had a threshold set to 5% of peak value.

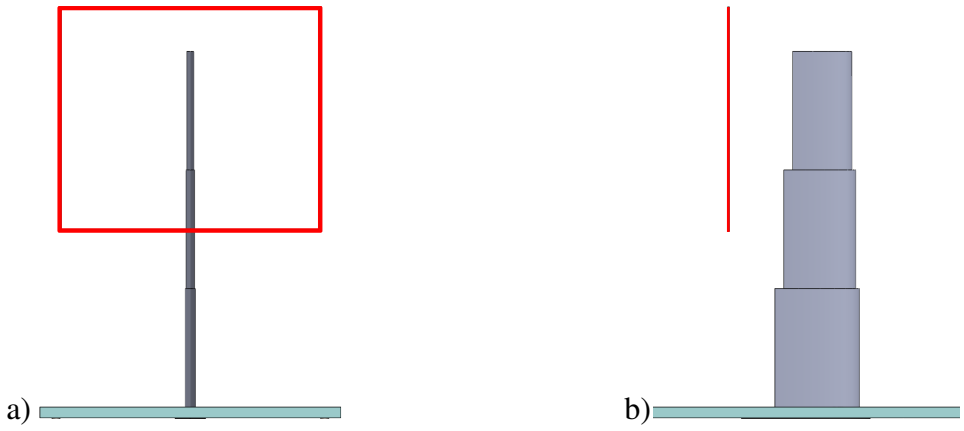

Fig. 3 a) Rear and b) top views of the PIV field of view.

IV. Results and Discussion

A. Force Balance Lift and Drag Measurements

Time-averaged force data presented in Figs.4-7 show no measurable difference in C_L, C_D, and L/D between the stepped and smooth wing shapes at α below stall. Despite a boundary layer trip on the suction surface, the $C_L(\alpha)$ curve at small α show some non-linearity. Near stall, the continuous wing generates a hysteresis loop. Greater lift and less drag were produced when the continuous wing was pitching up, in comparison to the wing pitching down. The 3 step wing abruptly stalled at $\alpha = 11°$, while the continuous wing stalled suddenly near $\alpha = 13°$ when pitching up and $\alpha = 11°$ when pitching down. The 7 step wing, however, experienced a gradual stall at about $\alpha = 11°$. The difference in stall behavior may be attributed to the presence of streamwise vortices shed at the steps. Under a crossflow, the effect of these vortices may change.

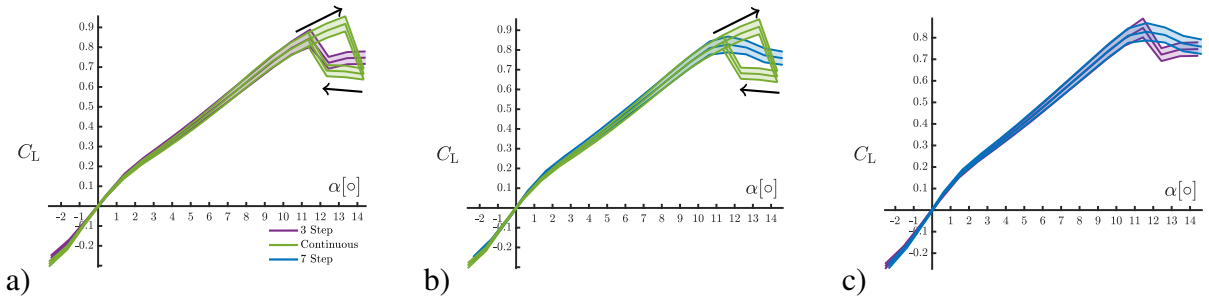

Fig. 4 Comparisons of C_L versus α between a) 3 step and continuous, b) 7 step and continuous, and c) 7 and 3 step wings. Data are plotted with shaded uncertainty envelopes.

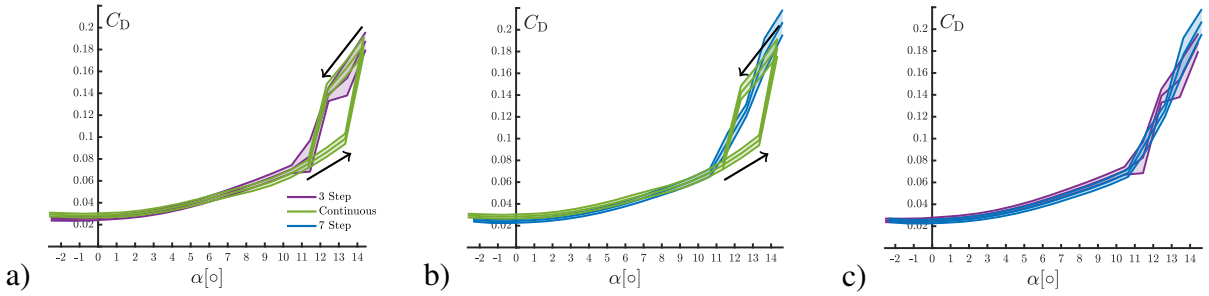

Fig. 5 Comparisons of C_D versus α between a) 3 step and continuous, b) 7 step and continuous, and c) 7 and 3 step wings. Plotting conventions as in previous figure.

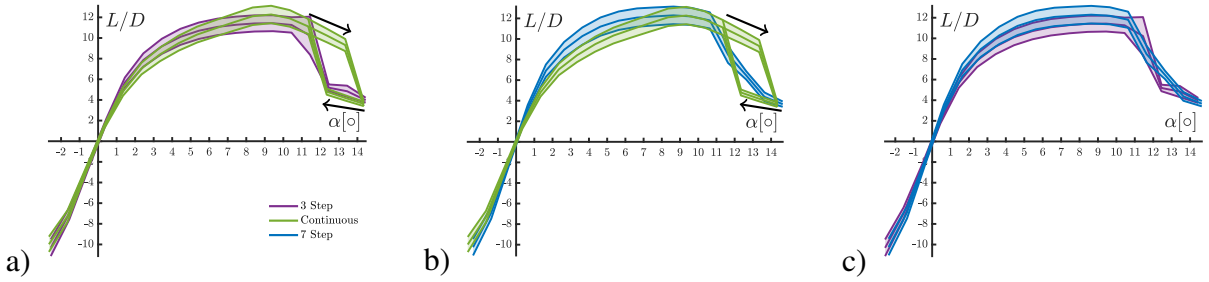

Fig. 6 Comparisons of L/D versus α between a) 3 step and continuous, b) 7 step and continuous, and c) 7 and 3 step wings.

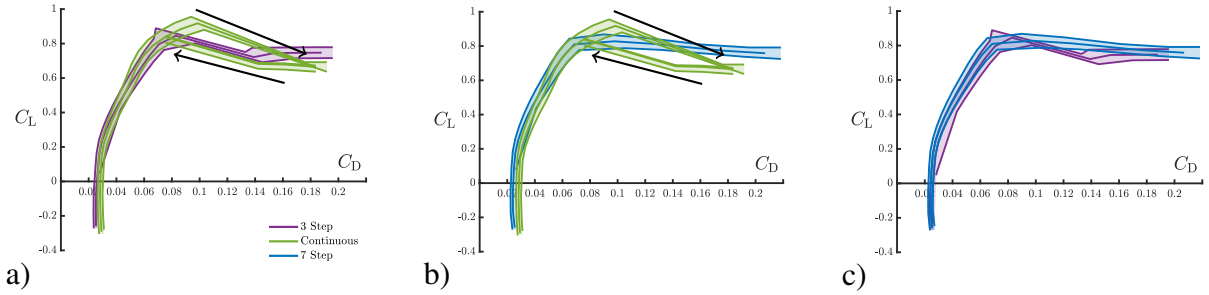

Fig. 7 Comparisons of C_L versus C_D between a) 3 step and continuous, b) 7 step and continuous, and c) 7 and 3 step wings.

The influence of a crossflow on time averaged forces is estimated in Figs.8-11. No measurable difference was observed in C_L or C_D before the onset of stall. Both the 3 step and 7 step wings showed a more gradual stall, and the hysteresis loop in lift of the continuous wing shrunk. The stall angle remained roughly the same between the swept and unswept cases though the stall angle was higher for the continuous wing in pitch-down. Because a flight vehicle will likely experience a crossflow, this robust stall behavior is desirable for vehicle design.

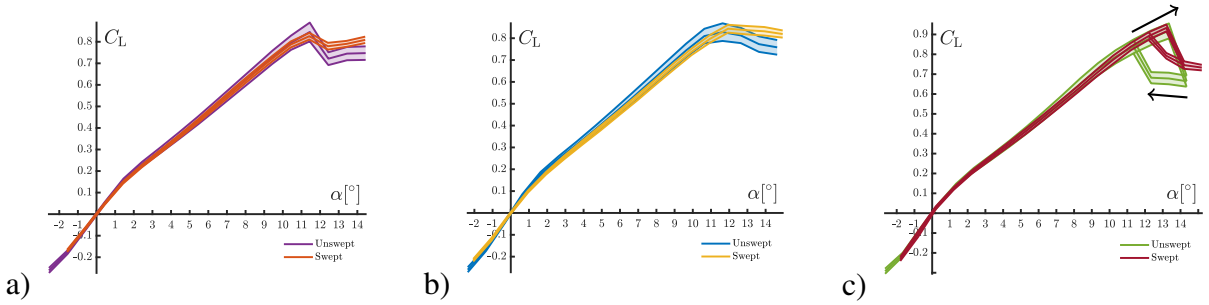

Fig. 8 C_L versus α for swept and unswept configurations. a) 3 step b) 7 step and c) continuous wings

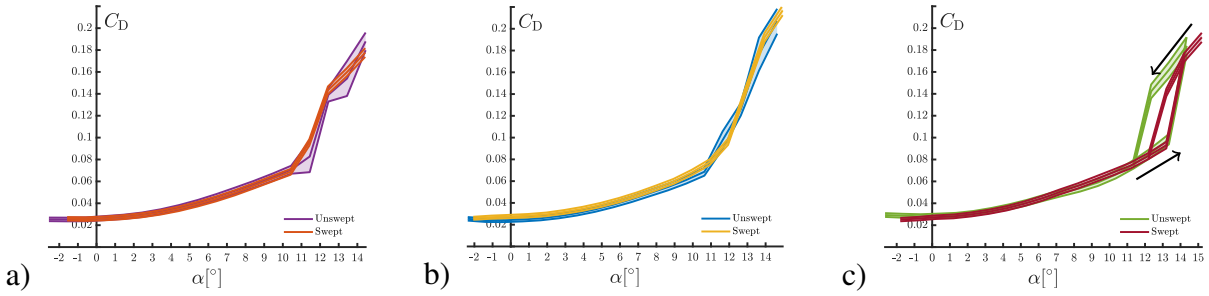

Fig. 9 C_D versus α for swept and unswept configurations. a) 3 step b) 7 step and c) continuous wings

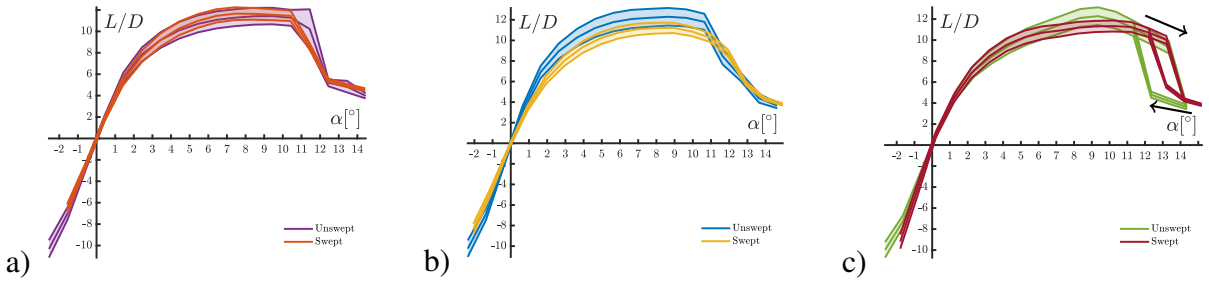

Fig. 10 L/D **versus** α **for swept and unswept configurations. a) 3 step b) 7 step and c) continuous wings**

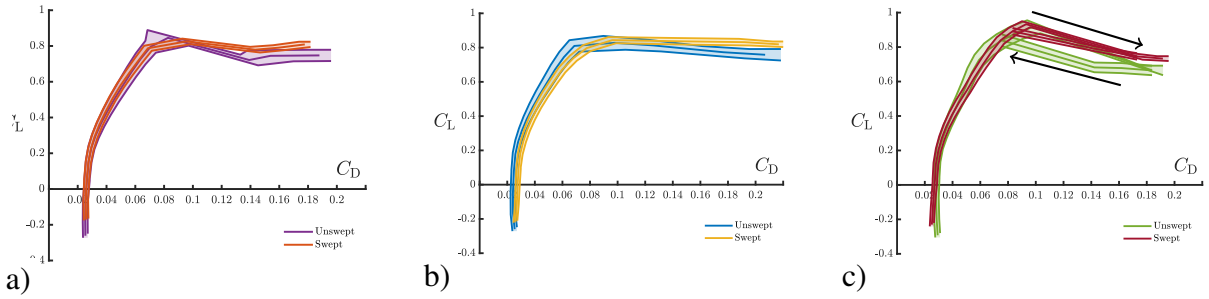

Fig. 11 C_L **versus** C_D **for swept and unswept configurations. a) 3 step b) 7 step and c) continuous wings**

B. Flow Visualization

From the Kutta-Joukowski theorem, the lift per unit span, L', is

$$L'(y) = \rho U \Gamma(y) \, , \tag{6}$$

where Γ is the bound circulation at span location y. The normalised circulation is directly related to the section lift coefficient as

$$C_\ell(y) = 2\frac{\Gamma}{Uc} \, . \tag{7}$$

Under conditions where a large fraction of the bound circulation is deposited into a wake which then rolls up into a concentrated vortex, then concentrations of streamwise vorticity can be integrated over selected areas, A, to estimate a wake circulation, which may then be related to the total circulation and hence lift on the wing:

$$\Gamma_w = \int \omega_x \mathrm{d}A \, . \tag{8}$$

Here, we may compare estimates of Γ_w in windows that encompass the tip vortex alone, or all measurable shed vorticity. In principle. streamwise vorticity is shed into the wake wherever there is a spanwise (or timewise) change in Γ. With large local Δc at the discontinuities of the 3 and 7 step wings, there will be a large $\Delta\Gamma$, which may lead to a recognizable structure in the wake.

PIV measurements presented in Figs. 12 and 13 show the presence of a concentrated wingtip vortex at $y/b = 1$ at both α. At higher α, the tip vortex is larger, commensurate with the higher total lift on the wing. One may also observe traces of a distinct vortical structure at the discontinuity of the 3 step wing at $y/b = 0.67$. This structure becomes larger when α is increased. No clear vortices were observed behind the discontinuities of the 7 step wing at $\alpha = 5°$. In Fig. 13b, there are bulges in the ω_x near the two steps closest to the wing tip. Though their amplitudes of ω_x are similar to vorticity shed in the same regions on the continuous wing, these concentrations of vorticity indicate the formation of a distinct structure. Streamwise vorticity was shed along the entire span of the continuous wing in the observation

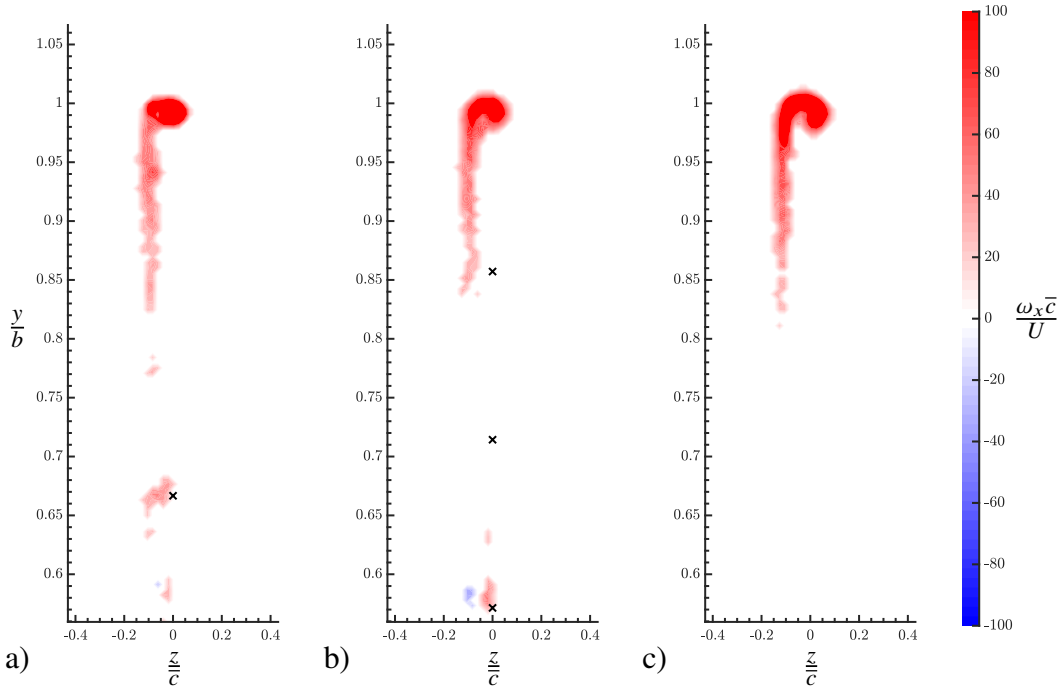

Fig. 12 Cross-stream plane of streamwise vorticity $0.75\overline{c}$ downstream of the a) 3 step, b) 7 step, and c) Continuous wings at $\alpha = 5°$. X mark denotes wing discontinuity locations.

	$\alpha = 5°$			$\alpha = 9°$		
Wing	Tip	Inboard	Total	Tip	Inboard	Total
3 Step	0.038	0.025	0.063	0.094	0.050	0.145
7 Step	0.032	0.023	0.055	0.101	0.053	0.154
Cont.	0.048	0.023	0.071	0.099	0.051	0.151

Table 1 Estimates of dimensionless circulation, $\Gamma/U\overline{c}$.

window at $\alpha = 9°$. Note that all measurements are at $x/c = 0.75$ from the wing trailing edge, and the viscous roll-up process is unlikely to be complete.

Based on the PIV measurements and Eqn. 8, estimates of $\Gamma/U\overline{c}$, are given in Table 1. The likely measurement uncertainty, $\Delta\Gamma$, was estimated from the maximum of the precision of any sequence of Γ between multiple PIV data sets of a given configuration, and evaluated to $\Delta\Gamma = 0.005$. As a reference, the resolution in setting any specified α is about 0.3°. For a wing with a lift slope $C_{L\alpha} = 2\pi\frac{\mathcal{AR}}{\mathcal{AR}+2}$ the expected variation in C_L is ±0.02, and through eq.7 the variation in $\Gamma/U\overline{c}$ would be on the order of 0.01. Within these uncertainty limits, none of the wake vortex strengths and circulations vary as wing geometry changes, though the expected variation in all cases with increasing α is detectable. Given the dispersed distributions of ω_x and the thresholding operation that will neglect all low-amplitude components, the wake circulations would be under-estimates of wing circulation, and we use them here only in a comparative way.

The only measured differences in the wings above from force balance data was in stall behavior. The hysteresis loop shown in both the unswept and swept cases of the continuous wing is typically associated with the formation and bursting of laminar separation bubbles. This was unexpected due to the boundary layer trip on the suction surface. Possibly, the presence of vortices at the wing discontinuities induced spanwise flow preventing the formation of these bubbles. When the continuous wing was swept, the hysteresis loop may have shrunk due to the presence of spanwise flow. Additional PIV experiments would be needed to confirm this hypothesis.

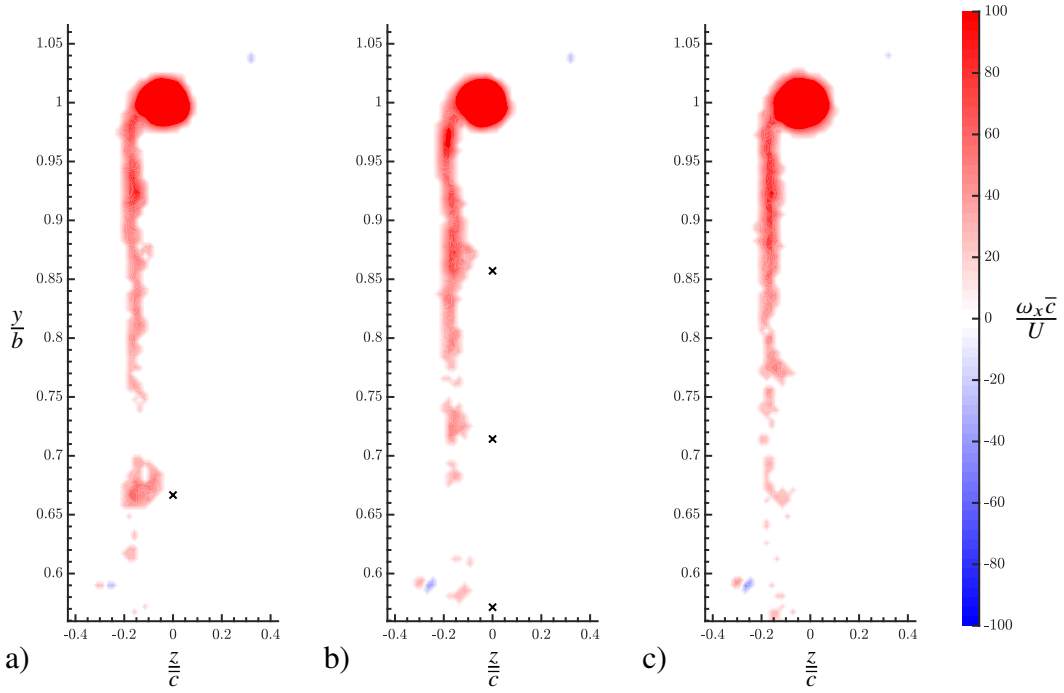

Fig. 13 Cross-stream plane of streamwise vorticity $0.75\bar{c}$ downstream of the a) 3 step,b) 7 step, and c) Continuous wings at $\alpha = 9°$. X mark denotes wing discontinuity locations.

V. Conclusion

Stepped and continuous wings were studied at Re $\approx 74,000$. Force balance measurements revealed no performance degradation for 3 step or 7 step wings compared with a continuous, tapered wing for α typical of aircraft cruise. Experiments were repeated for wings swept 10° to examine the effect of a sideslip angle. The hysteresis loop in the lift curve of the continuous wing shrunk, while the stepped wings showed a more gradual stall in a crossflow. A vortical structure was found at the discontinuity of the 3 step wing in the wake but no similar structures were measurable in the wake of the 7 step wing. Though step discontinuities were associated with shedding of streamwise vorticity, the integrated effect across the span was negligible, in agreement with direct force balance measurements.

Acknowledgments

The work presented here was performed under an on-going AFOSR Phase II STTR entitled "Biomimetic Design of Morphing UAVs," with Concepts-to-Systems, Inc., as the prime contractor and University of Southern California as a subcontractor. We would like to thank Dr Les Lee, the AFOSR Program Manager, for his support and guidance. USC undergraduates Haya Helmy, Patrick Valadez, and Stephen Douglass are thanked for their assistance in the printing and testing of wind tunnel models.

References

[1] Laitone, E., "Wind tunnel tests of wings at Reynolds numbers below 70 000," *Experiments in Fluids*, Vol. 23, No. 5, 1997, pp. 405–409. doi:10.1007/s003480050128.

[2] Mueller, T. J., and Batil, S. M., "Experimental studies of separation on a two-dimensional airfoil at low Reynolds numbers," *AIAA journal*, Vol. 20, No. 4, 1982, pp. 457–463. doi:10.2514/3.51095.

[3] Yarusevych, S., Sullivan, P. E., and Kawall, J. G., "On vortex shedding from an airfoil in low-Reynolds-number flows," *Journal of Fluid Mechanics*, Vol. 632, 2009, pp. 245–271. doi:10.1017/s0022112009007058.

[4] Selig, M. S., Guglielmo, J. J., Broeren, A. P., and Giguére, P., *Summary of Low-Speed airfoil data*, Vol. 1, SoarTech, 1995.

[5] McGhee, R. J., Walker, B. S., and Millard, B. F., "Experimental results for the Eppler 387 airfoil at low Reynolds numbers in the Langley low-turbulence pressure tunnel," Tech. rep., 1988.

[6] Simons, M., and Simons, M., *Model aircraft aerodynamics*, Nexus Special Interests Hemel Hempstead, UK, 1999.

[7] Tank, J., Smith, L., and Spedding, G., "On the possibility (or lack thereof) of agreement between experiment and computation of flows over wings at moderate Reynolds number," *Interface focus*, Vol. 7, No. 1, 2017, p. 20160076. doi:10.1098/rsfs.2016.0076.

[8] Hanna, Y. G. T., and Spedding, G. R., "Aerodynamic Performance Improvements Due to Porosity in Wings at Moderate Re," *AIAA Aviation 2019 Forum*, Dallas, TX, 2019.

[9] Pennycuick, C. J., "Gliding Flight of the Fulmar Petrel," *Journal of Experimental Biology*, Vol. 37, No. 2, 1960, pp. 330–338.

[10] Rosén, M., and Hedenström, A., "Gliding Flight in a Jackdaw: A Wind Tunnel Study," *Journal of Experimental Biology*, Vol. 204, No. 6, 2001, pp. 1153–1166.

[11] Lentink, D., Müller, U. K., Stamhuis, E. J., De Kat, R., Van Gestel, W., Veldhuis, L. L. M., Henningsson, P., Hedenström, A., Videler, J. J., and Van Leeuwen, J. L., "How Swifts Control their Glide Performance with Morphing Wings," *Nature*, Vol. 446, No. 7139, 2007, p. 1082.

[12] Di Luca, M., Mintchev, S., Heitz, G., Noca, F., and Floreano, D., "Bioinspired Morphing Wings for Extended Flight Envelope and Roll Control of Small Drones," *Interface focus*, Vol. 7, No. 1, 2017, p. 20160092. doi:10.1098/rsfs.2016.0092.

[13] Barbarino, S., Bilgen, O., Ajaj, R. M., Friswell, M. I., and Inman, D. J., "A Review of Morphing Aircraft," *Journal of intelligent material systems and structures*, Vol. 22, No. 9, 2011, pp. 823–877. doi:10.1177/1045389X11414084.

[14] Hanna, Y., Spedding, G., West, M., Kornbluh, R., Kirkwood, G., and Kudva, J., "Enabling Biomimetic Morphing UAVs," *22nd International Conference on Composite Materials*, Melbourne, Australia, 2019.

[15] Samuel, J. B., and Pines, D. J., "Design and Testing of a Pneumatic Telescopic Wing for Unmanned Aerial Vehicles," *Journal of Aircraft*, Vol. 44, No. 4, 2007, pp. 1088–1099. doi:10.2514/1.22205.

[16] Blondeau, J., Richeson, J., and Pines, D., "Design of a Morphing Aspect Ratio Wing Using an Inflatable Telescoping Spar," *44th AIAA/ASME/ASCE/AHS/ASC Structures, Structural Dynamics, and Materials Conference*, Norfolk, VA, 2003, p. 1718. doi:10.2514/6.2003-1718.

[17] Yue, T., Zhang, X., Wang, L., and Ai, J., "Flight Dynamic Modeling and Control for a Telescopic Wing Morphing Aircraft via Asymmetric Wing Morphing," *Aerospace Science and Technology*, Vol. 70, 2017, pp. 328–338. doi:10.1016/j.ast.2017.08.013.

[18] Henry, J. J., Blondeau, J. E., and Pines, D. J., "Stability Analysis for UAVs with a Variable Aspect Ratio Wing," *46th AIAA/ASME/ASCE/AHS/ASC Structures, Structural Dynamics and Materials Conference*, Austin, TX, 2005, p. 2044. doi: 10.2514/6.2005-2044.

[19] Fish, F. E., Weber, P. W., Murray, M. M., and Howle, L. E., "The Tubercles on Humpback Whales' Flippers: Application of Bio-Inspired Technology," *Integrative and Comparative Biology*, Vol. 51, No. 1, 2017, pp. 203–213. doi:10.1093/icb/icr016.

[20] Zabat, M., Frascaroli, S., Browand, F., Nestlerode, M., and Baez, J., "Drag Measurements on a Platoon of Vehicles," Tech. rep., 1994.